Comptes Rendus

Chimie

Dominique Bazin, Vincent Frochot, Jean-Philippe Haymann, Emmanuel Letavernier and Michel Daudon

Crystal size in *µ*crystalline pathologies and its clinical implication

Microcrystalline pathologies: Clinical issues and nanochemistry / *Pathologies microcristallines : questions cliniques et nanochimie*

Crystal size in μcrystalline pathologies and its clinical implication

Dominique Bazin [*], [a], **Vincent Frochot** [b, c], **Jean-Philippe Haymann** [b, c], **Emmanuel Letavernier** [b, c] **and Michel Daudon** [b, c]

[a] Université Paris-Saclay, CNRS, Institut de Chimie Physique, 91405 Orsay cedex, France

[b] AP-HP, Hôpital Tenon, Service des explorations fonctionnelles, 75020 Paris, France

[c] Unité INSERM UMR S 1155, UPMC, Hôpital Tenon, 75020 Paris, France

E-mails: dominique.bazin@universite-paris-saclay.fr (D. Bazin),
vincent.frochot@aphp.fr (V. Frochot), Jean-Philippe.haymann@aphp.fr
(J.-P. Haymann), emmanuel.letavernier@aphp.fr (E. Letavernier),
michel.daudon@aphp.fr (M. Daudon)

Abstract. Chemical composition is not the only information establishing a significant link between kidney stones and the pathology which induces urolithiasis. Structural parameters such as morphology and crystal and crystallite size are also of primary importance. In this contribution, we would like to assess the relationship of crystal size of different chemical phases with the pathology underlying such calcifications. Based on literature as well as on some of our measurements, we will appreciate the value of this structural parameter for different crystalline species in various clinical or biological conditions and in helping the clinician, especially to understand why bacterial imprints in infection-related stones are only visible in calcium phosphate apatite deposits.

Keywords. Lithiasis, X-ray diffraction, Infection, Bacteria, Imprints.

Published online: 28 July 2021

1. Introduction

Microcrystalline pathology is an exciting research field [1–10] in which most investigations have been performed on the mineral component of the biological deposits induced by the pathology. With respect to urolithiasis, the morphoconstitutional model defines the morphology of the kidney stones as one of the key parameters to establish a link between the kidney stone and the pathology which has induced it [11–18].

For several years, we have been describing the morphology and the size of the crystallites and nanocrystals which constitute the kidney stone (KS). From a physicochemical point of view, we used the terms "nanocrystals" and "crystallites" according to Van Meerssche and Feneau-Dupont [19] in order to define the structural hierarchy of these mineral concretions. Crystallites (measuring typically some tens of micrometers) are made of a collection of crystals (measuring typically some hundreds of nanometers).

At the mesoscopic scale, the morphology and size of crystallites can be determined by scanning electron microscopy (SEM) [6,20,21], while at the nanometric scale, the size of crystals is determined by X-ray scattering [22–24], powder neutron diffraction (PND) [25,26], X-ray absorption spectroscopy [27–31] or by transmission electron microscopy [32–36].

In this contribution, we would like to review the crystal size of the principal chemical compounds identified in kidney stones namely calcium oxalate, calcium phosphate, uric acid, struvite, and cystine. This structural parameter is of primary importance in the case of pathological calcifications. For example, it is related to their toxicity [37–39]. The cooperative effects of Na^+ and citrates on the dissolution of calcium oxalate crystals can be also be discussed in terms of this structural parameter [40].

We have selected papers which have focussed on measurement of crystal size and discuss the implication of this structural parameter in medical research.

2. Determination of crystal size

Numerous excellent publications and books have been dedicated to X-ray scattering [22–24,41–44]. Scattering occurs whenever electromagnetic radiation interacts with matters. As underlined by Woolfson [41], X-ray scattering can be thought of as due to the absorption of incident radiation with subsequent re-emission. Such re-emission consists of two components. One has the same wavelength (equivalent to energy) as the incident radiation and is called Thomson scattering. The second one has a longer wavelength (or a lower energy) than that of the incident radiation with a difference of wavelength depending on the angle of scatter. Here, we will focus on the Thomson scattering.

In the case of a crystal, the scattered radiation from each atom is coherent with respect to that from all others (Figure 1).

The Debye scattering equation elegantly relates the scattering intensity to the geometry of the crystal [45–52].

$$I(q) = \sum_i \sum_j f_i(q) f_j(q) \sin(qR_{ij})/qR_{ij}$$

In this equation, $I(q)$ is the angle dependent intensity (q is the momentum transfer, i.e. $q = 4\pi \sin\theta/\lambda$) from Thomson scattering, the sums
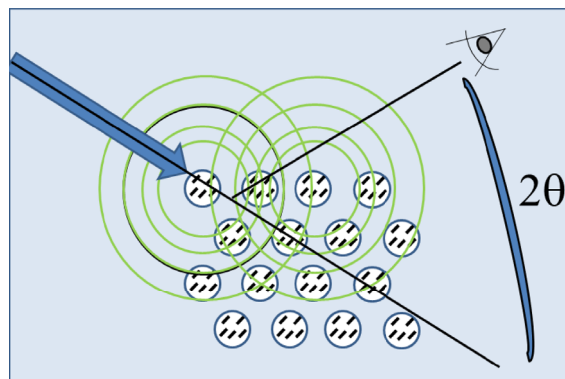

Figure 1. As pointed out by Cassetta [42], when the electromagnetic wave (blue arrow) interacts with atomic electrons, a secondary wave (with the same wavelength) is scattered in all directions by the atom itself (green circles). The secondary waves produced by the three-dimensional regular array of atoms give rise to interference phenomena which can be destructive or constructive depending on the disposition of the atoms relative to the incident radiation. At the angle of 2θ, constructive interference X-ray scattering peaks are observed.

over i and j are over all the atoms, R_{ij} is the distance between the atoms i and j, and f_i and f_j are the angle dependent atomic scattering factors. This equation neglects thermal disorder as well as Compton scattering, as a first approximation. A significant point relevant to this equation is the fact that the scattering factors, which take into account the interaction between X-rays and matter, have been tabulated by Sasaki [53] and that R_{ij} can be obtained easily from a structural model of the crystal [54–64].

Figure 2 shows the use of the Debye scattering equation to calculate the scattering intensity corresponding to face centered cubic (fcc) nanometer-scale platinum clusters of different sizes (represented by different numbers, N, of atoms).

For a cluster containing 13 atoms, the scattering peaks are very broad, exemplifying the fact that X-ray scattering is best suited for materials with long range order. Furthermore the figure also shows that the scattering peak width depends significantly on the size of the cluster.
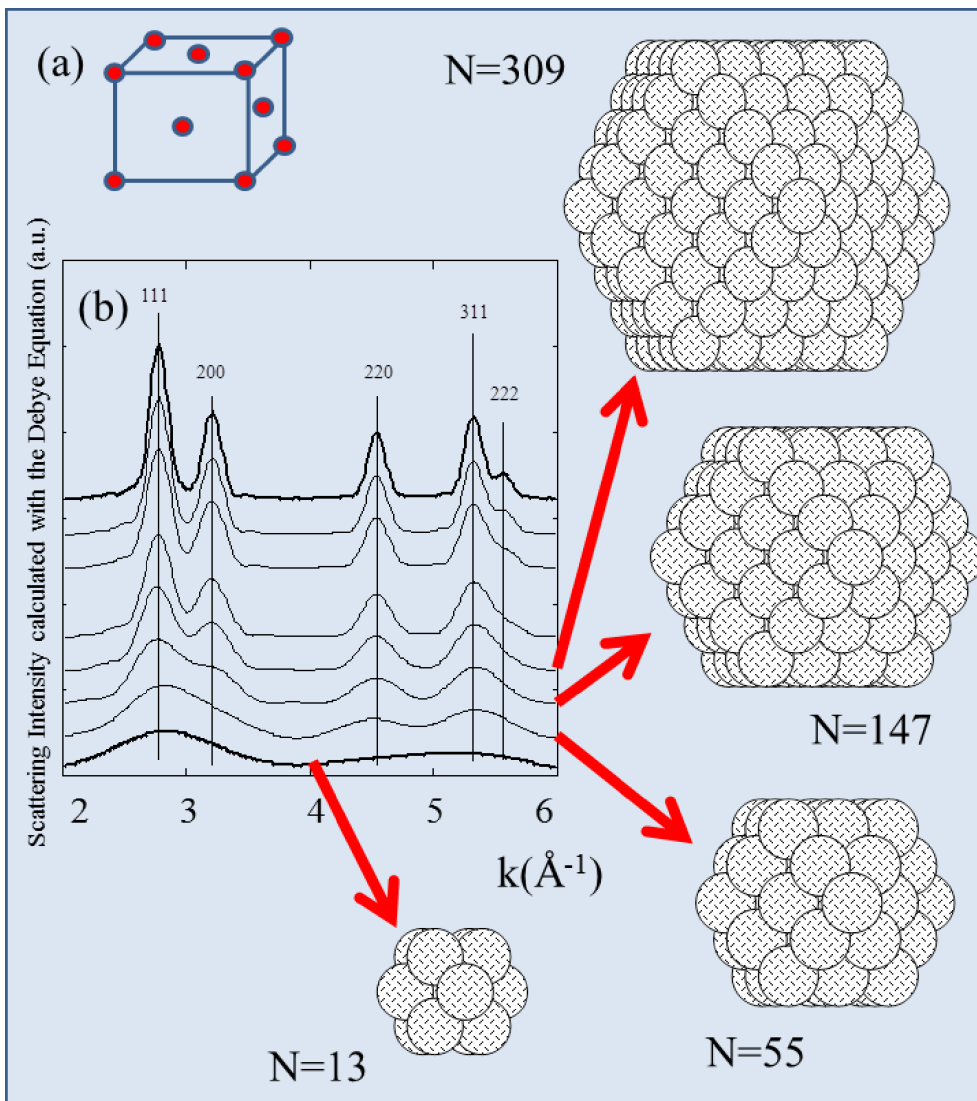
For a nanometer-scale cluster with a "spherical"

Figure 2. (a) Simple scheme for a fcc arrangement of atoms. (b) Diffraction diagram calculated for fcc nanometer-scale clusters of *N* platinum atoms.

morphology the amplitude of all the intensities are equivalent (Figure 2). This is not the case for asymmetric structures such as nanotubes (Figure 3). X-ray diffraction is thus very sensitive to the size and the morphology of nanometer-scale clusters, especially for monodisperse population.

Miranda and Sasaki [65] pointed out that the Scherrer or Debye–Scherrer equation [66,67] can be used to obtain nanocrystal size (D) from X-ray powder diffraction measurements by a simple relationship between D, the full width at half-maximum (Θ)

of the diffraction peak, the Bragg angle (θ_B) and the wavelength of the radiation (λ) [68]. k is a dimensionless number of the order of unity [69], known as the Scherrer constant, after Scherrer [66] who first used this method of estimating crystallite sizes.

$$\Theta \approx k\lambda / D \cos(\theta_B)$$

This equation assumes that the incoming scattered radiation does not interact with other atoms ("kinematical" or "geometrical" theory of X-ray diffraction). Bear in mind that the Scherrer
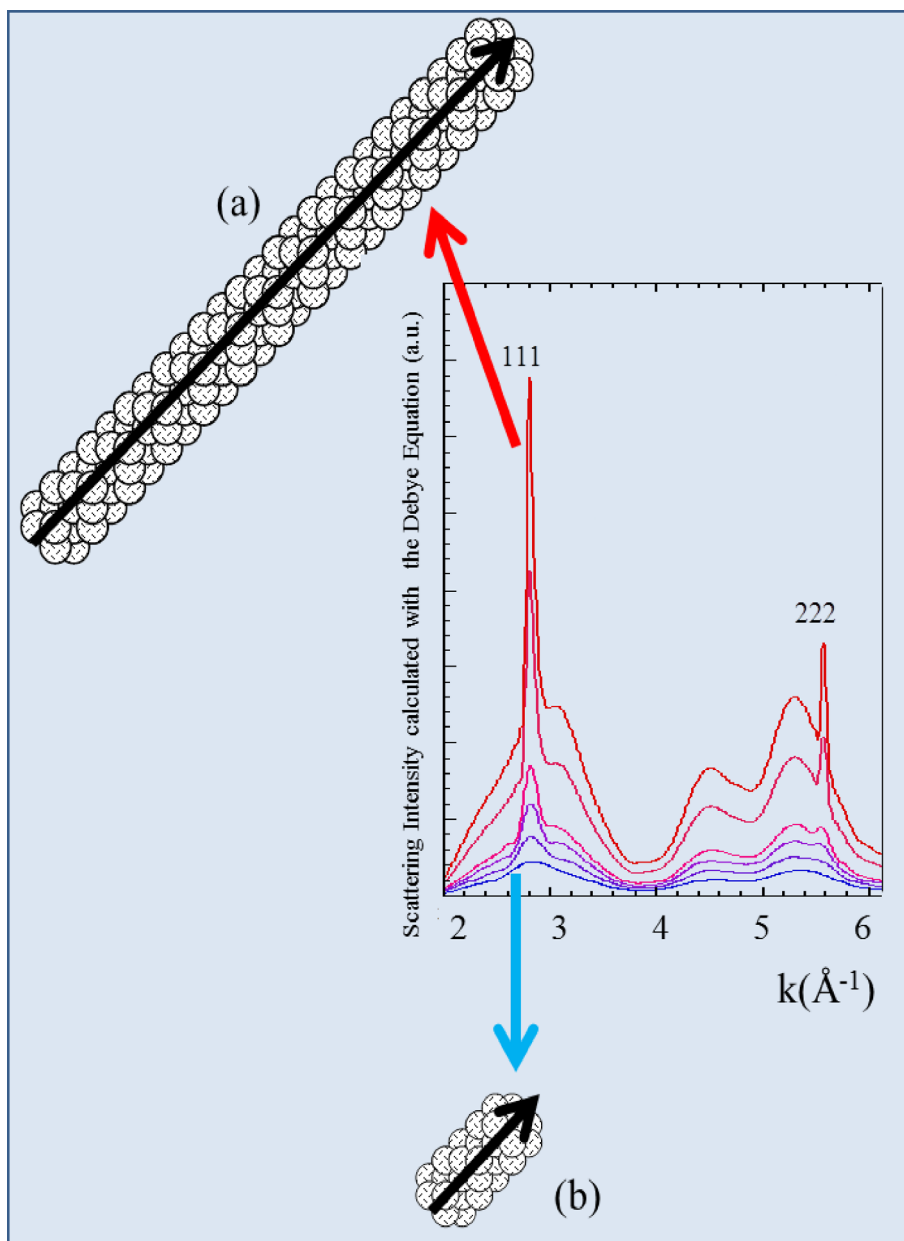
Figure 3. The diffraction peaks of a nanotube display different widths (a) and (b). The 111 direction which corresponds to the long axis of the nanotube is associated with the sharpest diffraction peak.

equation does not take into account the type or scattering power of the atoms, the crystal symmetry, or the reflection used. Despite all the simplifications, the size of nanometer crystals yielded is very similar to those obtained by other techniques. Londoño-Restrepo *et al.* [70] have measured the

nanocrystal sizes obtained by the analysis of X-ray scattering diagrams using Scherrer's equation and the analysis of images by High Resolution Transmission Electron Microscopy. The nanocrystal sizes for raw samples obtained by both methods are mutually consistent, which confirms that Scherrer's
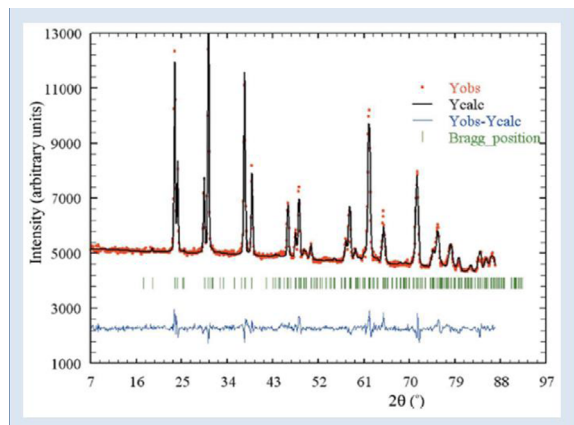
Figure 4. Final refinement, with experimental (circles), calculated (dashes), and difference PND patterns of the sample T11283. Tick marks below the profiles indicate the peak positions of allowed Bragg reflections for whewellite [71].

equation is an excellent tool to determine the size for nanocrystals. There is also excellent agreement between theoretical calculations of the scattering intensity by nanometer-scale clusters using the Debye equation [45–52] and the Scherrer law.

3. The case of calcium oxalate monohydrate KS

According to the morphoconstitutional model [11–18], five main subtypes, namely Ia, Ib, Ic, Id and Ie of calcium oxalate monohydrate kidney stones exist. All have been investigated by SEM and Neutron Diffraction or Powder Neutron Diffraction (PND) [71]. Neutrons are electrically neutral and interact only weakly with matter, and thus have a penetration depth of several centimeters [72]. In Figure 4, we show the final refinement, with experimental (circles), calculated (dashes), and difference PND patterns of the sample N11283. The mean sizes of the nanocrystals in these five subtypes (range 75–125 nm) were 107 nm (Ia), 80 nm (Ib), 110 nm (Ic), 90 nm (Ic) and 105 nm (Ie). These values are consistent with the investigation of Uvarov *et al.* [73]. If the crystal sizes are similar but the subtypes are different, the structural characteristics of the crystallites differ considerably [74]. Figure 5 shows the distinctive morphology of the calcium oxalate form crystallites for Ia (a), Ic (b) and Ie (c).
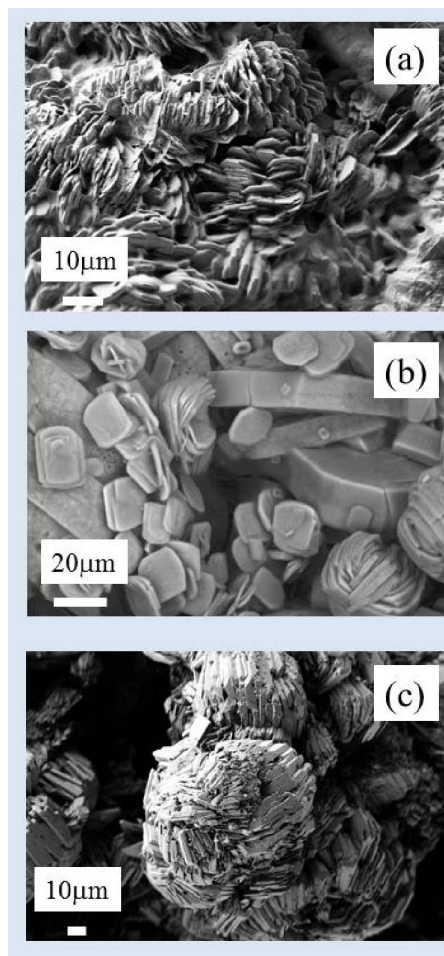

Figure 5. Peculiar morphology for COM crystallites in the case of Ia (a), Ic (b) and Ie (c) subtype (hyperoxaluria).

4. The case of calcium oxalate dihydrate (COD) crystals

Calcium oxalate crystals found in urine samples of stone formers range from 0.5 to 85 µm in size. Indeed, crystal size seems to be related to urine biochemistry. As shown in Figure 6, we found that among 5427 urine samples containing COD crystals, the mean size of the crystals is slightly increasing according to the calcium oxalate molar product (pCaOx). By contrast, the maximal size measured for COD crystals in urine is tenfold higher when pCaOx increased from 2.28 to 4.26 (mmol/l)[2].
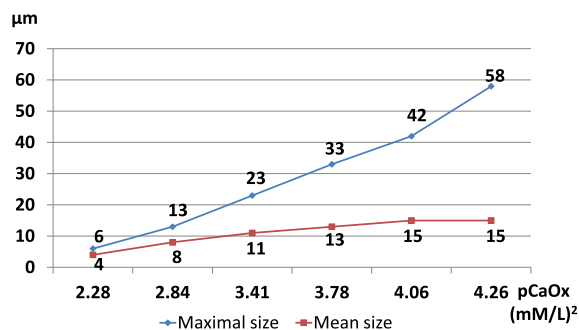
Figure 6. Size of calcium oxalate dihydrate crystals found in urine according to the calcium oxalate molar product.

5. The case of calcium phosphate apatite KS

Calcium phosphate in the form of carbapatite (CA) is a very common crystalline phase in urinary stones. Taking into account a large data bank including 50,000 stones acquired over the past three decades, CA has been identified by selective infrared analysis in 80% of all stones in both sexes, in most cases as a minor component [75]. It is worth underlining that despite its low proportion, CA is often clinically relevant as an initiating phase of the lithogenic process, as observed in stones developed from a Randall's plaque [76–81].

XRD as well as PND experiments have been performed on CA typical of physiological (bones) as well as pathological (Randall's plaque) calcifications [85–87]. Moreover, using atomic force microscopy, Eppell *et al.* [82] have obtained direct three-dimensional visual evidence of the size and shape of native protein-free mineralites isolated from mature bovine bone. Data analysis show that approximately 98% of the crystals are less than 2 nm thick displaying a plate-like habit. In Figure 7, the authors contrast the thicknesses (a), the widths (b), and the lengths (c), of the small mineralites.

These structural characteristics are consistent with our PND (Figure 8) and XRD experiments (Figure 9). Figure 8 illustrates several kinds of samples [83]. High temperature calcinated stoichiometric synthetic hydroxyapatites are characterized by a neutron diffraction diagram with sharp diffraction peaks because the size of the crystal is typically around a few micrometers (see Figure 2 for rationalization). In the case of synthetic nanocrystalline
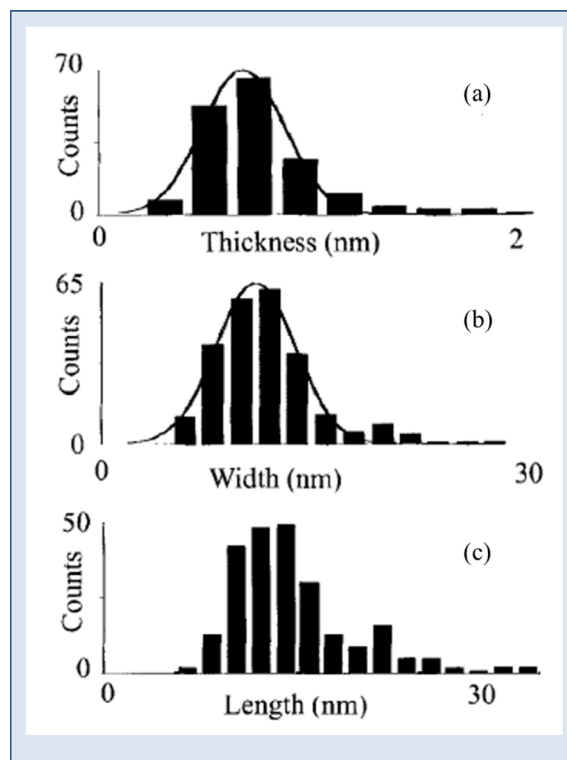

Figure 7. Histograms of AFM assessed dimensions of small protein-free mineralites from bone. The dimensions were normally distributed: best-fit Gaussians were superimposed on each histogram: (a) thicknesses (b) widths (c) lengths [82].

apatites, the diffraction peak widths are more significant because the size of the crystals is around several nanometers, except the 002 diffraction peak which indicates the anisotropy of the platelet-like nanocrystals of all these compounds. Finally, PND diagrams of physiological apatites are very similar to those of synthetic nanocrystalline apatites [88–91].

At the micrometer scale, SEM shows that the plate-like crystals are agglomerated and appear as spherical structures (Figure 9).

6. The case of struvite KS

Struvite (magnesium ammonium phosphate hexahydrate) stones form as a result of UTI (Urinary Tract Infection) by urease-producing pathogens and are thus often referred to as infection stones [92–96]. As pointed out by Flannigan *et al.* [93], struvite
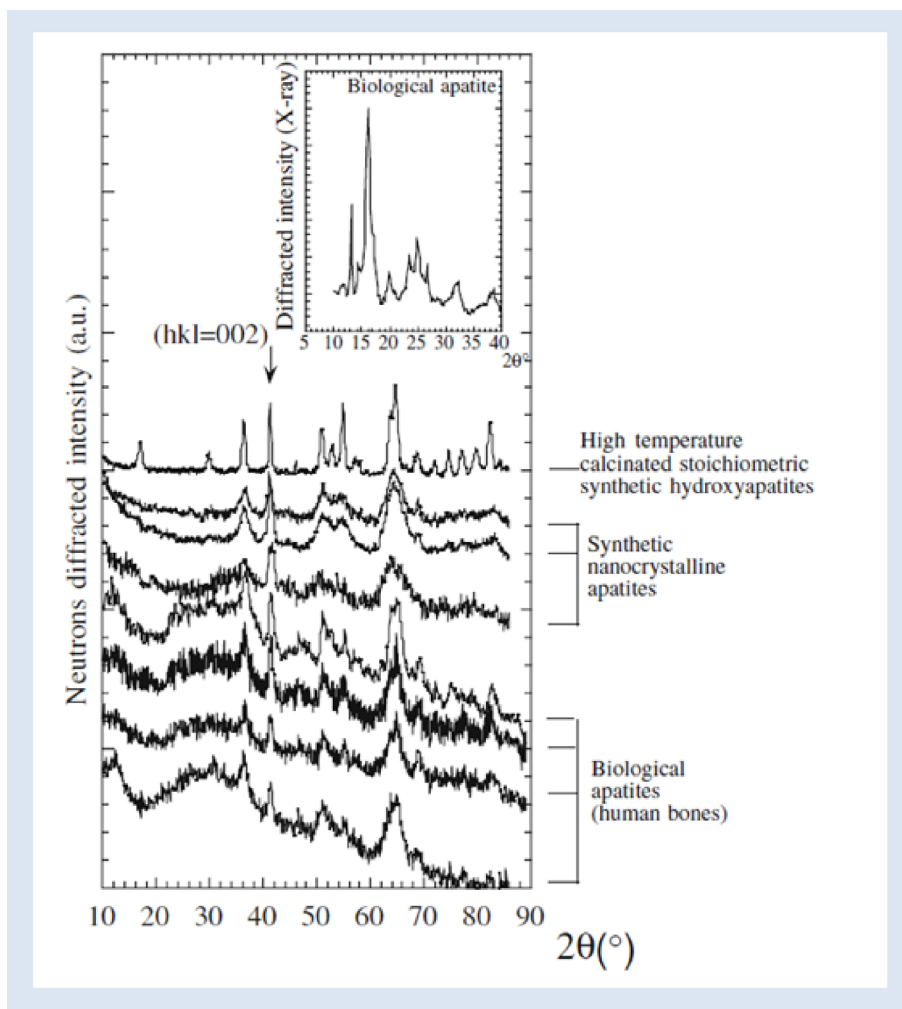
Figure 8. Neutron diffractograms of three families of apatite: high temperature calcinated synthetic apatite, room-temperature synthetic apatites and biological apatites (bones). The insert shows a corresponding X-ray diffractogram [83].

stone formation is exclusively associated with both gram-positive and gram-negative urease-producing species.

To explain the absence of bacterial imprints at the surface of struvite crystallites [84,97], PND experiments have been performed. As Figure 10 shows, the diffraction peaks of the struvite stone (stone T33776) are significantly sharper than those of nanocrystalline CA (stone T21934), indicating that the size of struvite crystals is much more significant than that of CA crystals. The data analysis indicates a struvite crystal mean size of 250 nm±25 nm, close to the maximum value that can be measured with our devices.

Note that, at the micrometer scale, struvite crystallites (Figure 11) display a typical specific 3-branch star surface morphology, in agreement with previous studies [98–100].

7. The case of whitlockite KS

Among phosphates, the species most frequently associated with infection are whitlockite [101,102], especially in women, and struvite in both male and female patients ($p < 0.0001$ vs. calcium oxalates in both sexes). Moreover calcium phosphate stones containing more than 30% whitlockite are associated with UTI in 81% of cases.
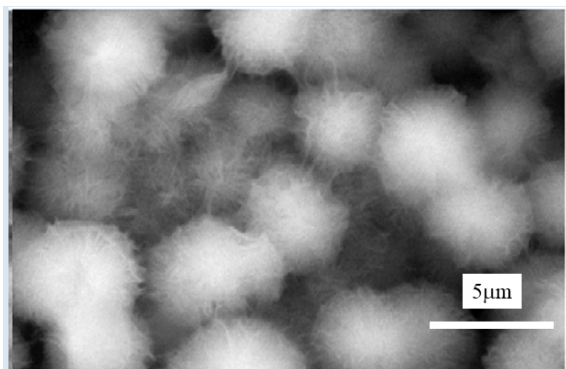
Figure 9. SEM of spherical CA entities in a kidney stone.

Table 1. Whitlockite crystal size for different kidney stones as measured by synchrotron XRD

Kidney stone	Crystal size
T32616	290 nm ± 10 nm
T38952	90 nm ± 10 nm
T43068	30 nm ± 10 nm
T43736	250 nm ± 10 nm
T45449	330 nm ± 10 nm
T51263	330 nm ± 10 nm
T52975	130 nm ± 10 nm
T55785	190 nm ± 10 nm
T74647	90 nm ± 10 nm
T74808	120 nm ± 10 nm

Recently, we have performed a set of X-ray scattering experiments using synchrotron radiation as a probe on the CRISTAL beamline of the Soleil synchrotron [103]. Thanks to recent advances [104,105] it was possible to perform a complete Rietveld analysis to obtain crystal sizes of whitlockite in different kidney stones [106]. The results are summarized in Table 1.

The average is around 185 nm, a much more significant value than reported for CA but quite similar to those of other chemical phases.

At the micrometer scale, whitlockite pseudo cubic crystallites are observed by SEM, a morphology consistent with their crystallographic structure [106,107].

8. The case of uric acid KS

As observed by Kenny and Goldfarb [108], with the proportion of obese Americans increasing and the association of obesity with low urine pH, uric acid nephrolithiasis is of paramount importance to the nephrologist, rheumatologist, and internist. Regarding prevalence, roughly 10% of stones in the United States are uric acid [109]. Between 1996 and 2007, a significant increase in the incidence of kidney stones in the pediatric population has been observed and such increases seem to be linked to the concomitant rise in obesity [110,111].

In a recent investigation, we have considered uric acid anhydrous (UAA) kidney stones and have measured their crystal size by neutron diffraction (Figure 13) [112].

This structural parameter was significantly different between male and female patients (84.7 ± 5.3 nm vs. 140.2 ± 6.7 nm, $p = 0.000003$). One of the striking points of this investigation is the fact that when type 2 diabetes develops, this structural difference between male and female vanished (76.1 ± 3.9 nm vs. 78.8 ± 4.2 nm, not significant).

Finally, on Figure 14, we can see a specific structure corresponding to the phase conversion between the two uric acid species (from dihydrate to anhydrous). Such observation is in line with the publication of Grases *et al.* [114] which has described the composition and structure of a set of uric acid stones and considers in vitro investigation of the crystallization behavior of uric acid.

9. The case of cystine KS

Cystinuria, an inheritable autosomal recessive disorder of amino acid transport, affects the epithelial cells of the renal tubules as well as the gastrointestinal tract [115–117]. This genetic pathology is characterized by abnormal concentrations of cystine and the other dibasic amino acids in the urine, leading to the formation of cystine renal stones because of the low solubility of cystine in urine [118,119]. It is the most frequent genetic cause of stone formation. Although two genes have been identified as causing this disease (SLC3A1 and SLC7A9), other unknown genes may also be involved in cystinuria [120,121].

The goal of the neutron scattering experiments (Figure 15) we have performed on cystine kidney
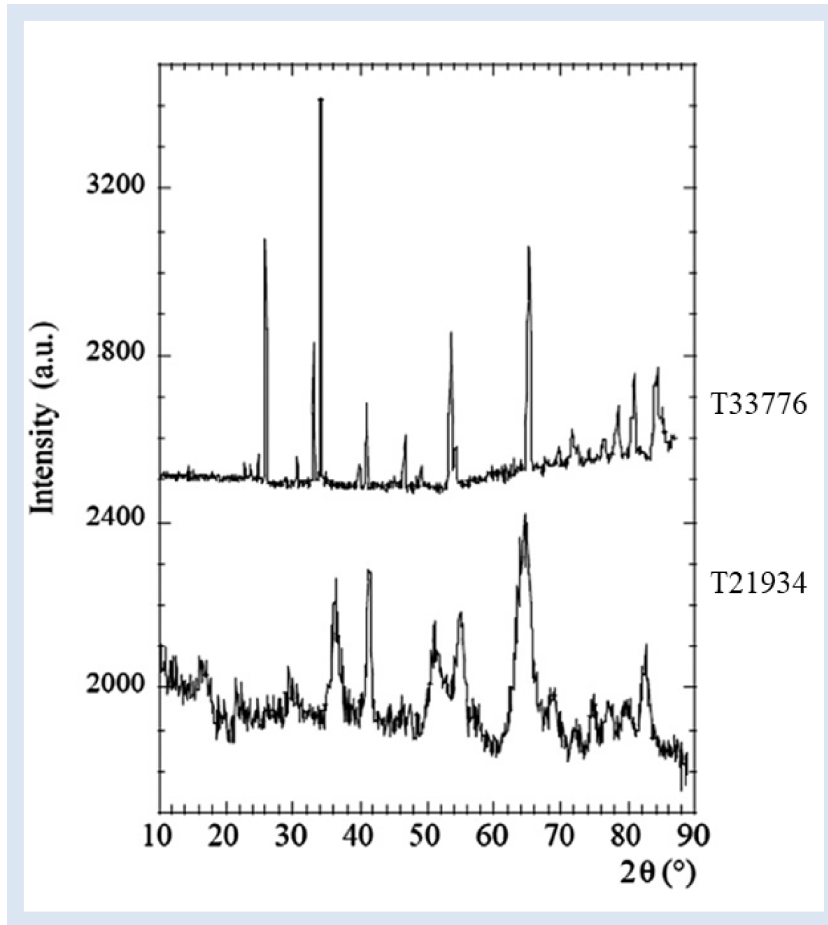
Figure 10. Neutron diffraction diagrams [84] collected for selected samples (T33776: struvite stone, T21934: calcium carbonated apatite stone).
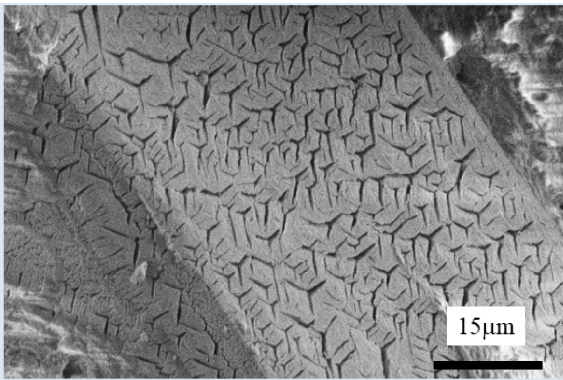

Figure 11. Typical morphologic features of struvite crystallites. Note the absence of bacterial imprints [84].

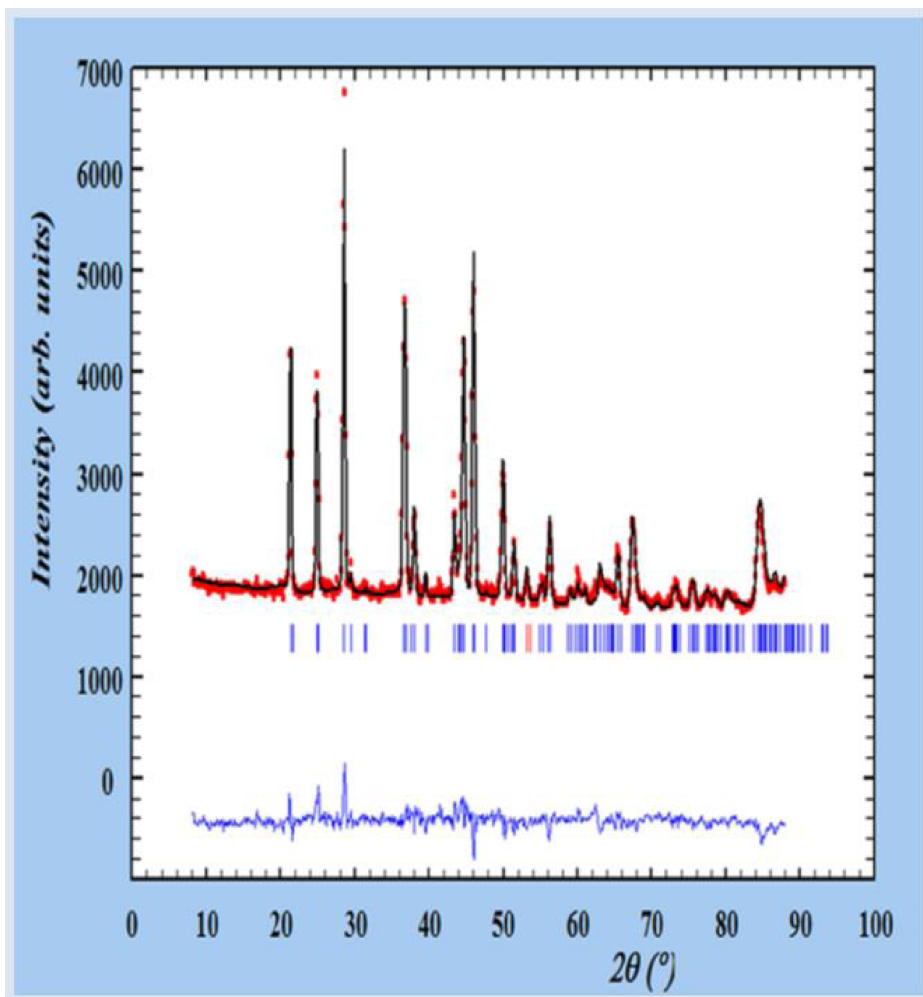**Figure 12.** SEM images of whitlockite crystallites.

Figure 13. Final refinement, with experimental (red points), calculated (black line) and their difference (blue line), obtained for the kidney stone T40161. Tick marks below the profiles indicate the peak positions of allowed Bragg reflections for UAA [112].
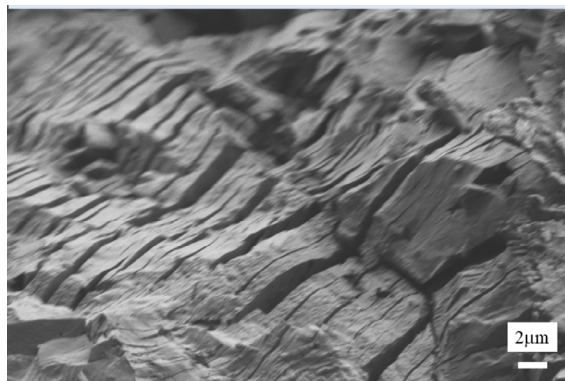
Figure 14. SEM images of uric acid kidney stones.

stones was to determine if medical treatment significantly modifies the size of cystine crystals [113]. The neutron data indicate clearly that treatment based on alkalinization by sodium bicarbonate significantly reduces the size of cystine crystals, from about 200 nm to about 120 nm. Moreover, as Figure 16 shows, alkalinization significantly modifies cystine crystallite morphology.

10. Discussion

The crystal structural characteristics of pathological calcifications constitute a key medical parameter for e.g. their toxicity [122]. For example, Sun *et al.* [38]

Figure 15. Typical observed (Y_{obs} in red), calculated (Y_{calc} in black), and difference, profiles ($Y_{obs}-Y_{calc}$ in blue) of the PND diagram of a cystine kidney stone. Tick marks (Bragg position in green) below the profiles indicate the peak positions of allowed Bragg reflections for cystine [113].
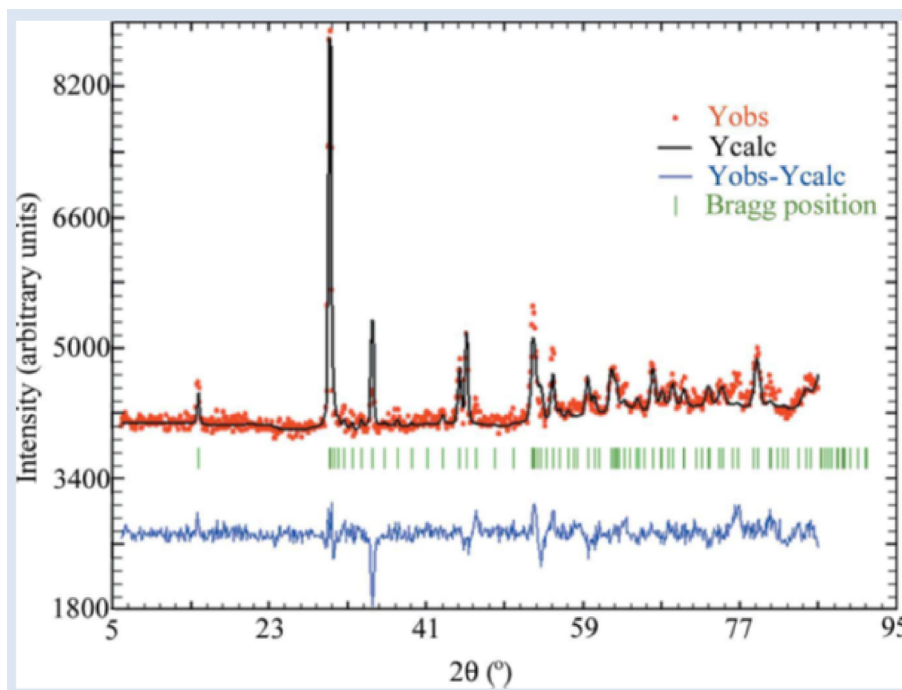
have demonstrated that crystal shapes and aggregation states are crucial factors affecting crystal toxicity in renal epithelial cells. In a previous study, the same group [37] also showed that nano-sized COM and COD crystals induced much greater cell death (sum of apoptosis and necrosis) than micron-sized crystals. With respect to hydroxyapatite (HAP), a recent investigation shows that nanoscale HAP-40 nm and HAP-70 nm were more toxic to HK-2 cells than the micron-sized HAP-1 μm [123]. Note that for HAP, the crystal morphology is also a major structural parameter in regard to inflammation process [124]. Crystal structural parameters can also be related to physiological parameters or developmental processes. For example, Leventouri *et al.* [125] have noted that the crystallinity of dental hydroxyapatite decreases with tooth age. Also, it is worth emphasizing that enamel crystallinity also exerts effects on mammalian and vertebrate dental evolution [126]. Finally, the importance of the size and morphology of crystal in perturbation of biological tissues has been noted for other chemical phases including calcium pyrophosphate [127] and monosodium urate [128].

The various results we have presented show clearly that the crystal size associated with the different solid chemical phases identified in urine i.e. calcium oxalate monohydrate (COM or whewellite), struvite, whitlockite, uric acid and cystine is around 100 nm while the crystal size of calcium phosphate apatite is generally around 30 nm. Such results are consistent with previous publications showing the same differences between crystal sizes of calcium phosphate apatite, and other chemical phases [47,129]. For example, Uvarov *et al.* [73] highlight that weddellite crystal size was always greater than that of whewellite when they were simultaneously present, while brushite exhibits the largest crystallites of all.

From a physicochemical point of view, the comparison between the size measured by XRD via the Scherrer law, and the SEM observations, presents an opportunity to discuss the difference between the size of a crystal as measured by SEM observations and what is in fact measured by the Scherrer law i.e. the coherently scattering domain size. For example, in the cases of whitlockite (Figure 12)
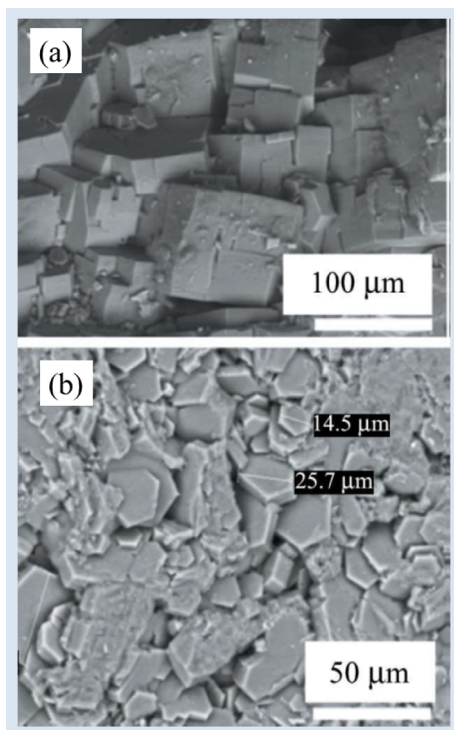
Figure 16. (a) SEM image of a typical Va cystine kidney stone made of large crystals exhibiting flat surfaces with well-defined corners and edges. The stone was removed from the kidney of an untreated patient. (b) SEM image of a Vb kidney stone [113].

and cystine (Figure 16a), well-defined edges and surfaces are clearly visible, giving the impression that micrometer-scale crystals are visualized and not crystallites. In fact, for these chemical phases, the difference between the coherently scattering domain size on a hundreds of nanometer scale, and the size of crystallites, indicates the presence of numerous structural defects which induce loss of long range order.

From a clinical point of view, we have mentioned that the crystal size is a key parameter in understanding interactions with cells. Differences in crystal size between calcium phosphate apatite and the other chemical phases is also of primary importance in understanding the localization of bacterial imprints, structural features which have been observed at the surface of concretions arising in various organs. Several papers have discussed the presence of bacterial imprints at the surface of kidney stones [84,97, 130,131], in prostatic stones [132,133], and of concretions in the bile duct [134]. In the case of prostate and kidney, the bacterial imprints were observed at the surface of the calcium phosphate apatite components of the concretions. None were observed at the surface of struvite crystallites although struvite is clearly related to urinary tract infection. To explain this apparent contradiction, we use the analogy of a man walking on a beach [84]. If the beach is sandy he leaves footprints, but not if the beach is stony. Bacterial imprints may thus appear in the small calcium carbonated apatite nanocrystals rather than in the large struvite ones. As shown for uric acid, COD or cystine, the size of either nanocrystals or of crystallites may be relevant to correlate biological crystals and biochemistry or medical treatment or pathological conditions.

11. Conclusion

Using examples from literature we have highlighted crystals and crystallite structural parameters of chemical phases identified in kidney stones by SEM and interpretation of XRD or PND diagrams. All reports point to the fact that the crystal size of most of the relevant chemical phases, namely calcium oxalate monohydrate (COM or whewellite), calcium oxalate dihydrate (COD or weddelite), brushite, struvite, whitlockite, uric acid, and cystine, is around 100 nm, whereas that of calcium phosphate apatite is predominantly around 30 nm.

These explain why bacterial imprints are only observed at the surface of calcium phosphate apatite kidney stones. Even though struvite is strongly associated with infection [135], its large crystal size can explain why bacterial imprints cannot form and be observed on the surface of struvite crystallites. Many of these observations around crystal size have clinical applications. SEM findings can thus help identify bacterial influences and better define urolithiasis etiology in patients generating kidney stones from which struvite is absent, and who give negative urine culture results and no evidence of fever.

Acknowledgments

References

[1] D. Bazin, M. Daudon, C. Combes, C. Rey, *Chem. Rev.*, 2012, **112**, 5092-5120.

[2] D. Bazin, M. Daudon, *J. Phys. D: Appl. Phys.*, 2012, **45**, article no. 383001.

[3] M. Daudon, D. Bazin, *J. Phys.: Conf. Ser.*, 2013, **425**, article no. 022006.

[4] L. N. Poloni, M. D. Ward, *Chem. Mater.*, 2014, **26**, 477-495.

[5] D. Bazin, J.-P. Haymann, E. Letavernier, J. Rode, M. Daudon, *Presse Med.*, 2014, **43**, 135-148.

[6] D. Bazin, M. Daudon, *Ann. Biol. Clin.*, 2015, **73**, 517-534.

[7] D. Bazin, E. Letavernier, J.-P. Haymann, P. Méria, M. Daudon, *Prog. Urol.*, 2016, **26**, 608-618.

[8] E. Tsolaki, S. Bertazzo, *Materials*, 2019, **12**, article no. 3126.

[9] D. Bazin, E. Letavernier, J. P. Haymann, V. Frochot, M. Daudon, *Ann. Biol. Clin.*, 2020, **78**, 349-362.

[10] N. Vidavsky, J. A. M. R. Kunitake, L. A. Estroff, *Adv. Healthc. Mater.*, 2020, article no. e2001271.

[11] M. Daudon, C. A. Bader, P. Jungers, *Scanning Microsc.*, 1993, **7**, 1081-1104.

[12] M. Daudon, *Arch. Pédiatr.*, 2000, **7**, 855-865.

[13] M. Daudon, P. Jungers, D. Bazin, *AIP Conf. Proc.*, 2008, **1049**, 199-215.

[14] V. Frochot, M. Daudon, *Int. J. Surg.*, 2016, **36**, 624-632.

[15] M. Daudon, *Prog. Urol.—FMC*, 2012, **22**, F87-F93.

[16] M. Daudon, O. Traxer, P. Jungers, *Lithiase Urinaire*, 2nd ed., Médecine-Sciences, Lavoisier, Paris, 2012, 672 pages.

[17] J. Cloutier, L. Villa, O. Traxer, M. Daudon, *World J. Urol.*, 2015, **33**, 157-169.

[18] M. Daudon, A. Dessombz, V. Frochot, E. Letavernier, J.-P. Haymann, P. Jungers, D. Bazin, *C. R. Chim.*, 2016, **19**, 1470-1491.

[19] M. Van Meerssche, J. Feneau-Dupont, *Introduction à la cristallographie Et à la chimie structurale*, Ed. Vander, Louvain, 1973.

[20] F. Brisset, M. Repoux, J. Ruste, F. Grillon, F. Robaut, *Microscopie Electronique à Balayage et Microanalyses*, EDP Sciences, 2009, ISBN: 978-2-7598-0082-7.

[21] M. Daudon, D. Bazin, "New techniques to characterize kidney stones and Randall's plaque", in *Urolithiasis: Basic Science and Clinical Practice* (J. J. Talati, H. G. Tiselius, D. M. Albala, Z. Ye, eds.), Springer, New York, 2012, 683-707.

[22] A. Guinier, *X-ray Diffraction in Crystals, Imperfect Crystals and Amorphous Bodies*, W.H. Freeman & Co., San Francisco, 1963.

[23] A. Guinier, *Théorie et technique de la radiocristallographie*, Dunod, Paris, 1964.

[24] A. Le Bail, H. Duroy, J. L. Fourquet, *Math. Res. Bull.*, 1988, **23**, 447-452.

[25] V. K. Pecharsky, P. Y. Zavalij, *Fundamentals of Powder Diffraction and Structural Characterization of Materials*, Springer-Verlag, New York, 2005.

[26] C. Kumar (ed.), *X-ray and Neutron Techniques for Nanomaterials Characterization*, Springer, Berlin, Heidelberg, 2016.

[27] D. E. Sayers, F. W. Lytle, E. A. Stern, *Adv. X-ray Anal.*, 1970, **13**, 248-271.

[28] E. A. Stern, D. E. Sayers, F. W. Lytle, *Phys. Rev. B*, 1975, **11**, 4836-4846.

[29] D. C. Bazin, D. A. Sayers, *Jpn. J. Appl. Phys.*, 1993, **32**, 249-251.

[30] D. C. Bazin, D. A. Sayers, *Jpn. J. Appl. Phys.*, 1993, **32**, 252-254.

[31] J. Moonen, J. Slot, L. Lefferts, D. Bazin, H. Dexpert, *Physica B*, 1995, **208**, 689-690.

[32] K. Nitiputri, Q. M. Ramasse, H. Autefage, C. M. McGilvery, S. Boonrungsiman, N. D. Evans, M. M. Stevens, A. E. Porter, *ACS Nano*, 2016, **10**, 6826-6835.

[33] C. Verrier, D. Bazin, L. Huguet, O. Stéphan, A. Gloter, M.-C. Verpont, V. Frochot, J.-P. Haymann, I. Brocheriou, O. Traxer, M. Daudon, E. Letavernier, *J. Urol.*, 2016, **196**, 1566-1574.

[34] C. Bardet, F. Courson, Y. Wu, M. Khaddam, B. Salmon, S. Ribes, J. Thumfart, P. M. Yamaguti, G. Y. Rochefort, M.-L. Figueres, T. Breiderhoff, A. GarciaCastaño, B. Vallée, D. Le Denmat, B. Baroukh, T. Guilbert, A. Schmitt, J.-M. Massé, D. Bazin, G. Lorenz, M. Morawietz, J. Hou, P. Carvalho-Lobato, M. C. Manzanares, J.-C. Fricain, D. Talmud, R. Demontis, F. Neves, D. Zenaty, A. Berdal, A. Kiesow, M. Petzold, S. Menashi, A. Linglart, A. C. Acevedo, R. Vargas-Poussou, D. Müller, P. Houillier, C. Chaussain, *J. Bone Miner. Res.*, 2016, **31**, 498-513.

[35] E. Bouderlique, E. Tang, J. Perez, A. Coudert, D. Bazin, M.-C. Verpont, C. Duranton, I. Rubera, J.-P. Haymann, G. Leftheriotis, L. Martin, M. Daudon, E. Letavernier, *Am. J. Pathol.*, 2019, **189**, 2171-2180.

[36] C. Gay, E. Letavernier, M.-C. Verpont, M. Walls, D. Bazin, M. Daudon, N. Nassif, O. Stephan, M. de Fruto, *ACS Nano*, 2020, **14**, 1823-1836.

[37] X.-Y. Sun, J.-M. Ouyang, W.-Y. Zhu, Y.-B. Li, Q.-Z. Gan, *J. Mater. Chem. B*, 2015, **3**, 1864-1878.

[38] X.-Y. Sun, Q.-Z. Gan, J.-M. Ouyang, *Cell Death Discov.*, 2015, **1**, article no. 15055.

[39] X.-Y. Sun, M. Xu, J.-M. Ouyang, *ACS Omega*, 2017, **2**, 6039-6052.

[40] M. Shanthil, K. Sandeep, P. K. Sajith, *Phys. Chem. Chem. Phys.*, 2020, **22**, 4788-4792.

[41] M. M. Woolfson, *An Introduction to X-ray Crystallography*, Cambridge Press, Cambridge, 1970.

[42] A. Cassetta, "X-ray diffraction (XRD)", in *Encyclopedia of Membranes* (E. Drioli, L. Giorno, eds.), Springer, Berlin, Heidelberg, 2014.

[43] B. E. Warren, *X-ray Diffraction*, Dover, New York, 1990.

[44] H. M. Rietveld, *J. Appl. Crystallogr.*, 1969, **2**, 65-71.

[45] P. J. W. Debye, *Ann. Phys.*, 1913, **348**, 49-92.

[46] P. J. W. Debye, *Ann. Phys.*, 1915, **351**, 809-823.

[47] A. Cervellino, C. Giannini, A. Guagliardi, *J. Appl. Crystallogr.*, 2003, **36**, 1148-1158.

[48] S. J. L. Billinge, I. Levin, *Science*, 2007, **316**, 561-565.

[49] L. Gelisio, P. Scardi, *Acta Crystallogr. A*, 2016, **72**, 608-620.

[50] P. Scardi, S. J. L. Billinge, R. Neder, A. Cervellino, *Acta Crystallogr. A*, 2016, **72**, 589-590.

[51] A. S. Vorokh, *Nanosyst. Phys. Chem. Math.*, 2018, **9**, 364-369.

[52] A. E. Ross, D. G. McCulloch, D. R. McKenzie, *Acta Crystallogr. A*, 2020, **76**, 468-473.

[53] S. Sasaki, *KEK Report 83-82*, National Laboratory for High Energy Physics, Tsukuba, Japan, 1983.

[54] D. Bazin, D. A. Sayers, J. J. Rehr, *J. Phys. Chem. B*, 1997, **101**, 11040-11050.

[55] D. Bazin, L. Guczi, J. Lynch, *Appl. Catal.*, 2002, **226**, 87-113.

[56] B. Ingham, *Crystallogr. Rev.*, 2015, **21**, 229-303.

[57] A. Cervellino, R. Frison, F. Bertolotti, A. Guagliardi, *J. Appl. Crystallogr.*, 2015, **48**, 2026-2032.

[58] F. Ferri, F. Bertolotti, A. Guagliardi, N. Masciocchi, *Sci. Rep.*, 2020, **10**, article no. 12759.

[59] D. Bazin, R. Revel, *J. Synchrotron Radiat.*, 1999, **6**, 483-485.

[60] R. Revel, D. Bazin, E. Elkaim, Y. Kihn, H. Dexpert, *J. Phys. Chem. B*, 2000, **104**, 9828-9835.

[61] D. Bazin, J. Lynch, M. Ramos-Fernandez, *Oil Gas Sci. Technol.—Rev. IFP*, 2003, **58**, 667-683.

[62] O. Ducreux, B. Rebours, J. Lynch, M. Roy-Auberger, D. Bazin, *Oil Gas Sci. Technol.—Rev. IFP*, 2009, **64**, 49-62.

[63] A. O. Bokuniaeva, A. S. Vorokh, *J. Phys.: Conf. Ser.*, 2019, **1410**, article no. 012057.

[64] F. Bertolotti, A. Vivani, D. Moscheni, F. Ferri, A. Cervellino, N. Masciocchi, A. Guagliardi, *Nanomaterials*, 2020, **10**, article no. 743.

[65] M. A. R. Miranda, J. M. Sasaki, *Acta Crystallogr. A*, 2018, **74**, 54-65.

[66] P. Scherrer, *Achr. Ges. Wiss. Göttingen*, 1918, **1**, 98-100.

[67] U. Holzwarth, N. Gibson, *Nat. Nanotechnol.*, 2011, **6**, 534.

[68] A. L. Patterson, *Phys. Rev.*, 1939, **56**, 978-982.

[69] J. I. Langford, A. J. C. Wilson, *J. Appl. Crystallogr.*, 1978, **11**, 102-113.

[70] S. M. Londoño-Restrepo, R. Jeronimo-Cruz, B. M. Millán-Malo, E. M. Rivera-Muñoz, M. E. Rodriguez-García, *Sci. Rep.*, 2019, **9**, article no. 5915.

[71] D. Bazin, M. Daudon, G. André, R. Weil, E. Véron, G. Matzen, *J. Appl. Crysallogr.*, 2014, **47**, 719-725.

[72] F. Damay, D. Bazin, M. Daudon, G. André, *C. R. Chim.*, 2016, **19**, 1432-1438.

[73] V. Uvarov, I. Popov, N. Shapur, T. Abdin, O. N. Gofrit, D. Pode, M. Duvdevani, *Environ. Geochem. Health*, 2011, **33**, 613-622.

[74] M. Daudon, P. Jungers, D. Bazin, *New Engl. J. Med.*, 2008, **359**, 100-102.

[75] M. Daudon, H. Bouzidi, D. Bazin, *Urol. Res.*, 2010, **38**, 459-467.

[76] A. Randall, *Ann. Surg.*, 1937, **105**, 1009-1027.

[77] M. Daudon, O. Traxer, P. Jungers, D. Bazin, *AIP Conf. Proc.*, 2007, **900**, 26-34.

[78] M. Daudon, O. Traxer, J. C. Williams, D. Bazin, "Randall's Plaque", in *Urinary Tract Stone Disease* (N. P. Rao, G. M. Preminger, J. P. Kavangh, eds.), Springer, New York, 2011, ISBN 978-1-84800-361-3.

[79] E. Letavernier, D. Bazin, M. Daudon, *C. R. Chim.*, 2016, **19**, 1456-1460.

[80] D. Bazin, E. Letavernier, C. Jouanneau, P. Ronco, C. Sandt, P. Dumas, G. Matzen, E. Véron, J.-P. Haymann, O. Traxe, P. Conort, M. Daudon, *C. R. Chim.*, 2016, **19**, 1461-1469.

[81] E. Letavernier, G. Kauffenstein, L. Huguet, N. Navasiolava, E. Bouderlique, E. Tang, L. Delaitre, D. Bazin, M. de Frutos, C. Gay, J. Perez, M. C. Verpont, J.-P. Haymann, V. Pomozi, J. Zoll, O. Le Saux, M. Daudon, G. Leftheriotis, L. Martin, *J. Am. Soc. Nephrol.*, 2018, **29**, 2337-2347.

[82] S. J. Eppell, W. Tong, J. L. Katz, L. Kuhn, M. J. Glimcher, *J. Orthop. Res.*, 2001, **19**, 1027-1034.

[83] D. Bazin, C. Chappard, C. Combes, X. Carpentier, S. Rouzière, G. André, G. Matzen, M. Allix, D. Thiaudière, S. Reguer, P. Jungers, M. Daudon, *Osteoporos. Int.*, 2009, **20**, 1065-1075.

[84] D. Bazin, G. André, R. Weil, G. Matzen, E. Véron, X. Carpentier, M. Daudon, *Urology*, 2012, **79**, 786-790.

[85] X. Carpentier, D. Bazin, C. Combes, A. Mazouyes, S. Rouzière, P.-A. Albouy, E. Foy, M. Daudon, *J. Trace Elem. Med. Biol.*, 2011, **25**, 160-165.

[86] U. Vetter, E. D. Eanes, J. B. Kopp, J. D. Termine, P. Gehron Robey, *Calcif. Tissue Int.*, 1991, **49**, 248-250.

[87] G. E. Bacon, A. E. Goodship, *J. Appl. Crystallogr.*, 2007, **40**, 349-353.

[88] S. Cazalbou, C. Combes, D. Eichert, C. Rey, M. J. Glimcher, *J. Bone Miner. Metab.*, 2004, **22**, 310-317.

[89] S. Cazalbou, D. Eichert, C. Drouet, C. Combes, C. Rey, *C. R. Palevol*, 2004, **3**, 563-572.

[90] C. Rey, C. Combes, C. Drouet, H. Sfihi, A. Barroug, *Mat. Sci. Eng. C*, 2007, **27**, 198-205.

[91] C. Drouet, C. Rey, in *Nanostructured Biomaterials for Regenerative Medicine* (V. Guarino, M. Iafisco, S. Spriano, eds.), Woodhead Publishing Series in Biomaterials, Elsevier, 2020.

[92] R. J. Reveillaud, M. Daudon, "Struvite stones analysis by infrared spectrophotometry in adults and children", in *Urolithiasis and Related Clinical Research* (P. O. Schwille, L. H. Smith, W. G. Robertson, W. Vahlensieck, eds.), Springer, Boston, MA, 1985.

[93] R. Flannigan, W. H. Choy, B. Chew, D. Lange, *Nat. Rev. Urol.*, 2014, **11**, 333-341.

[94] M. Daudon, P. Jungers, D. Bazin, J. C. Williams Jr., *Urolithiasis*, 2018, **46**, 459-470.

[95] M. A. P. Manzoor, B. Singh, A. K. Agrawal, A. B. Arun, M. Mujeeburahiman, P. D. Rekha, *PLoS One*, 2018, **13**, article no. e0202306.

[96] J. C. Williams Jr., A. J. Sacks, K. Englert, R. Deal, T. L. Farmer, M. E. Jackson, J. E. Lingeman, J. A. McAteer, *J. Endourol.*, 2012, **26**, 726-731.

[97] X. Carpentier, M. Daudon, O. Traxer, P. Jungers, A. Mazouyes, G. Matzen, E. Véron, D. Bazin, *Urology*, 2009, **73**, 968-975.

[98] A. N. Kofina, P. G. Koutsoukos, *Cryst. Growth Des.*, 2005, **5**, 489-496.

[99] J. Prywer, A. Torzewska, *Cryst. Growth Des.*, 2009, **9**, 3538-3543.

[100] J. Prywer, A. Torzewska, *Cryst. Res. Technol.*, 2010, **45**, 1283-1289.

[101] L. Maurice-Estepa, P. Levillain, B. Lacour, M. Daudon, *Scand. J. Urol. Nephrol.*, 1999, **88**, 299-305.

[102] F. A. Shah, *Acta Biomater.*, 2021, **125**, 72-82.

[103] D. Bazin, M. Daudon, E. Elkaim, A. Le Bail, L. Smrcok, *C. R. Chim.*, 2016, **19**, 1535-1541.

[104] S. Amirthalingam, A. Ramesh, S. S. Lee, N. S. Hwang, R. Jayakumar, *ACS Appl. Bio Mater.*, 2018, **1**, 1037-1046.

[105] T. Debroise, E. Colombo, G. Belletti, J. Vekeman, Y. Su, R. Papoular, N. S. Hwang, D. Bazin, M. Daudon, P. Quaino, F. Tielens, *Cryst. Growth Des.*, 2020, **20**, 2553-2561.

[106] D. Bazin, R. J. Papoular, E. Elkaim, R. Weil, D. Thiaudière, C. Pisapia, B. Ménez, N. S. Hwang, F. Tielens, M. Livrozet, E. Bouderlique, J.-P. Haymann, E. Letavernier, L. Hennet, V. Frochot, M. Daudon, *C. R. Chim.*, 2022, **25**, no. S1, 343-354.

[107] C. Frondel, *Am. Mineral.*, 1941, **26**, 145-152.

[108] J.-E. S. Kenny, D. S. Goldfarb, *Curr. Rheumatol. Rep.*, 2010, **12**, 125-129.

[109] N. S. Mandel, G. S. Mandel, *J. Urol.*, 1989, **142**, 1516-1521.

[110] L. Durner, A. Bourdoumis, N. Buchholz, *C. R. Chim.*, 2016, **19**, 1451-1455.

[111] D. J. Sas, *J. Pediatr.*, 2010, **157**, 132-137.

[112] M. Daudon, E. Letavernier, R. Weil, E. Véron, G. Matzen, G. André, D. Bazin, *C. R. Chim.*, 2016, **19**, 1527-1534.

[113] D. Bazin, M. Daudon, G. André, R. Weil, E. Véron, G. Matzen, *J. Appl. Crystallogr.*, 2014, **47**, 719-725.

[114] F. Grases, A. L. Villacampa, A. Costa Bauza, O. Sohnel, *Scanning Microsc.*, 1999, **13**, 223-234.

[115] A. Trinchieri, G. Dormia, E. Montanari, G. Zanetti, *Arch. Ital. Urol. Androl.*, 2004, **76**, 129-134.

[116] L. Dello Strologo, G. Rizzoni, *Acta Paediatr. Suppl.*, 2006, **95**, 31-33.

[117] A. Sahota, J. A. Tischfield, D. S. Goldfarb, M. D. Ward, L. Hu, *Urolithiasis*, 2019, **47**, 57-66.

[118] E. Letavernier, O. Traxer, J.-P. Haymann, D. Bazin, M. Daudon, *Prog. Urol.—FMC*, 2012, **22**, F119-F123.

[119] J. P. Haymann, M. Livrozet, J. Rode, S. Doizi, O. Traxer, V. Frochot, E. Letavernier, D. Bazin, M. Daudon, *Prog. Urol.—FMC*, 2021, **31**, F1-F7.

[120] L. Feliubadaló, M. L. Arbonés, S. Mañas, J. Chillarón, J. Visa, M. Rodés, F. Rousaud, A. Zorzano, M. Palacín, V. Nunes, *Hum. Mol. Genet.*, 2003, **12**, 2097-2108.

[121] M. Livrozet, S. Vandermeersch, L. Mesnard, E. Thioulouse, J. Jaubert, J.-J. Boffa, J.-P. Haymann, L. Baud, D. Bazin, M. Daudon, E. Letavernier, *PLoS ONE*, 2014, **9**, article no. e102700.

[122] S. R. Khan, *Urol. Res.*, 1995, **23**, 71-79.

[123] X.-Y. Sun, J.-Y. Chen, C.-Y. Rao, J.-M. Ouyang, *Int. J. Nanomedicine*, 2020, **15**, 5043-5060.

[124] F. Lebre, R. Sridharan, M. J. Sawkins, D. J. Kelly, F. J. O'Brien, C. Lavelle, *Sci. Rep.*, 2017, **7**, article no. 2922.

[125] T. Leventouri, A. Antonakos, A. Kyriacou, R. Venturelli, E. Liarokapis, V. Perdikatsis, *Int. J. Biomater.*, 2009, **2009**, article no. 698547.

[126] A. Kallistová, R. Skála, M. Šlouf, P. Čejchan, I. Matulková, I. Horáček, *Sci. Rep.*, 2018, **8**, article no. 5544.

[127] A. Swan, B. Heywood, B. Chapman, H. Seward, P. Dieppe, *Ann. Rheum. Dis.*, 1995, **54**, 825-830.

[128] M. A. Martillo, L. Nazzal, D. B. Crittenden, *Curr. Rheumatol. Rep.*, 2014, **16**, 400-408.

[129] P. Chatterjee, A. Chakraborty, A. K. Mukherjee, *Spectrochim. Acta Part A*, 2018, **200**, 33-42.

[130] L. Cifuentes Delatte, M. Santos, *Eur. Urol.*, 1977, **3**, 96-99.

[131] K. M. Englert, J. A. McAteer, J. E. Lingeman, J. C. Williams Jr, *Urolithiasis*, 2013, **41**, 389-394.

[132] A. Dessombz, P. Méria, D. Bazin, M. Daudon, *PLoS One*, 2012, **7**, article no. e51691.

[133] A. Dessombz, P. Méria, D. Bazin, E. Foy, S. Rouzière, R. Weil, M. Daudon, *Prog. Urol.*, 2011, **21**, 940-945.

[134] J. W. C. Leung, J. Y. Sung, J. W. Costerton, *J. Clin. Microbiol.*, 1989, **27**, 915-921.

[135] E. J. Espinosa-Ortiz, B. H. Eisner, D. Lange, R. Gerlach, *Nat. Rev. Urol.*, 2019, **16**, 35-53.